INTERNATIONAL JOURNAL FOR NUMERICAL METHODS IN FLUIDS, VOL. 27, 139–157 (1998)

LINEAR STABILITY OF INCOMPRESSIBLE FLUID FLOW IN A CAVITY USING FINITE ELEMENT METHOD

YAN DING AND MUTSUTO KAWAHARA*

Department of Civil Engineering, Chuo University, Kasuga 1-13-27, Bunkyo-ku, Tokyo 112, Japan

SUMMARY

Numerical methods have been applied to theoretical studies of instability and transition to turbulence. In this study an analysis of the linear stability of incompressible flow is undertaken. By means of the finite element method the two-dimensional base flow is computed numerically over a range of Reynolds numbers and is perturbed with three-dimensional disturbances. The partial differential equations governing the evolution of perturbation are obtained from the non-linear Navier–Stokes equations with a slight compressibility by using linear stability and normal mode analysis. In terms of the finite element discretization a non-singular generalized eigenproblem is formulated from these equations whose solution gives the dispersion relation between complex growth rate and wave number. This study presents stability curves to identify the critical Reynolds number and critical wavelength of the neutral mode and discusses the mechanism of instability. The stability of lid-driven cavity flow is examined. Taylor–Göertler-like vortices in the cavity are obtained by means of reconstruction of three-dimensional flows. © 1998 John Wiley & Sons, Ltd.

Int. J. Numer. Meth. Fluids, **27**: 139–157 (1998)

KEY WORDS: hydrodynamic stability; finite element method; incompressible cavity flow; Arnold's method

1. INTRODUCTION

The transition of fluid flow is a very complicated phenomenon which can be characterized only by means of many parameters, of which the Reynolds number *Re* is the most important. The stability of parallel flows such as plane Poiseuille and boundary layer flows, owing to the similarity of velocity profile in the streamwise direction, can be described by the Orr–Sommerfeld equation, which is at least a fourth-order ordinary differential equation. The neutral curve can be identified from the spatial modes or/and temporal modes by means of calculation of a generalized eigenproblem. The calculation of this eigenproblem is very complex even for the simplest canonical flows.[1]

Numerical methods have been applied to theoretical studies of instability and transition to turbulence since shortly after the advent of digital computers. A rationally asymptotic framework was developed for treating the linear and weakly non-linear stability of non-parallel flows by means of finite difference and spectral methods.[2,3] The linear theory is applicable to some transition problems and describes the first stage of transition—the (usually) slow growth of the primary instability. By means of three-dimensional disturbances on the primary instability wave the secondary instability can

* Correspondence to: M. Kawahara, Department of Civil Engineering, Chuo University, Kasuga 1-13-27, Bunkyo-ku, Tokyo 112, Japan.

CCC 0271–2091/98/010139–19 $17.50
© 1998 John Wiley & Sons, Ltd.
Received May 1996

also be analysed by a variety of numerical methods.

Kleiser and Zang[4] have reviewed the discretization in space and time of the Navier–Stokes equations by using finite difference, spectral and/or spectral domain decomposition methods. The precise choice of discretization in space is primarily a matter of efficiency and convenience. However, the numerical methods mentioned above are limited to quite simple geometries.[5–7] Using finite difference methods, a co-ordinate transformation is necessary in order to simulate even simple geometries such as the flow around a cylinder.[8,9] In contrast, using the finite element method, complex geometries can be described exactly and effectively.[10,11] Li and Kot,[10] like earlier practitioners, have analysed one-dimensional Poiseuille flow by the finite element method with Hermitian interpolation. Jackson[11] has discussed in detail the onset of vortex shedding in flow past variously shaped bodies by Newton–Raphson iteration. However, the matters of common concern are the accuracy, efficiency and convenience of various numerical methods.

The purpose of this study is to analyse the linear stability of incompressible flow by employing the finite element method, owing to the advantages of convenience and accuracy in the simulation of flows with complex geometries. As an example we focus on the linear stability of lid-driven cavity flow in which three-dimensional disturbances are allowed for. The main assumption of this study is that the cavity is of infinite axial extent, which allows for the eigenproblem to be decomposed into normal modes in the spanwise direction. To overcome the singularity of the eigenproblem in the linear analysis of incompressible flows,[12] we further employ a slight compressibility to eliminate the singularity. In addition, Khorrami *et al.*[6] stated that the effect on the desired (physical) eigenvalues was negligible. Ramanan and Homsy[2] have reviewed cavity flow from experimental and numerical studies. The main conclusion can be summarized by the following observation. It appears that the flow is most definitely two-dimensional below $Re = 500$. At some critical Reynolds number below 1000 there is a transition to a secondary state. Reliable experimental results are provided by Aidun *et al.*[13] in this range of Reynolds numbers. For our study the basic two-dimensional lid-driven cavity flow is computed by means of an improved velocity correction method whereby the continuity constraint can be satisfied perfectly.[14]

2. MATHEMATICAL FORMULATIONS

There are two routes to drive the mathematical formulations for the analysis of stability in incompressible fluid flows. One way is to form the non-linear Navier–Stokes equations with the continuity constraint.[2,12] Owing to this constraint, a singular eigenproblem results. Therefore, in general, definite potential functions are adopted to force the velocity field to be solenoidal and automatically satisfy the continuity equation.[15] This will result in a coupled set of fourth-order partial differential equations for the potentials.[2] Therefore, using the finite element discretization, the Hermitian interpolation function is needed at least, which implies that the total number of degrees of freedom will double. Thus this technique is inconvenient and time-consuming for the solution of such linear algebraic equations derived from the FEM.

Another method is to write the governing equations in primitive variable form in order to utilize the Lagrangian interpolation function for the finite element discretization. This will keep the linear algebraic system within the appropriate momory size. In this study we adopt this latter technique to form the discretized system by the FEM with a slight compressibility so as to eliminate the singularity in the eigenproblem.

 © 1998 John Wiley & Sons, Ltd.

2.1. Formulations

We consider lid-driven cavity flow in a cavity that is infinitely long in the spanwise direction, in which the motion of the fluid is driven by the top boundary moving at constant speed V_0, with width and height L. Let us assume that the fluid is slightly compressible, isothermal and Newtonian. In addition, the non-dimensional scales for length, velocity, time and pressure are L, V_0, L/V_0 and CV_0 respectively, where C is the acoustic speed in the fluid. The dimensionless form of the continuity equation for Newtonian fluid flow is

$$\frac{\mathrm{D}\rho}{\mathrm{D}t} + \rho\nabla\cdot\mathbf{v} = 0 \quad \text{in } \Omega, \tag{1}$$

where $\mathrm{D}/\mathrm{D}t$ denotes mass differentiation with respect to dimensionless time. Owing to the slight compressibility, given the pressure only as a function of density, for the kinematic pressure we have

$$\frac{\mathrm{D}p}{\mathrm{D}\rho} = \frac{1}{\rho}\frac{1}{Ma}\frac{\mathrm{D}\rho}{\mathrm{D}t}, \tag{2}$$

where $M_a = V_0/C$ is the Mach number in the fluid. Substituting (2) into (1), the modified continuity equation with the slight compressibility assumption can be written as

$$\frac{\mathrm{D}p}{\mathrm{D}t} + \frac{1}{Ma}\nabla\cdot\mathbf{v} = 0. \tag{3}$$

To derive the equation of motion, we consider the constitutive relation of the Newtonian fluid with the Stokes hypothesis as (in indicial form)

$$\tau_{ij} = -\frac{1}{Ma}p\delta_{ij} + 2Re^{-1}\left(S_{ij} - \frac{1}{3}\frac{\partial u_i}{\partial x_i}\delta_{ij}\right), \tag{4}$$

where $Re = \rho V_0 L/\mu$ is the Reynolds number in the cavity flow, with μ the viscosity of the fluid, and

$$S_{ij} = \frac{1}{2}\left(\frac{\partial u_i}{\partial x_j} + \frac{\partial u_j}{\partial x_i}\right). \tag{5}$$

Under the condition of slight compressibility, considering the viscosity μ of the fluid as constant, the non-dimensional momentum equations can be written as

$$\frac{\mathrm{D}\mathbf{v}}{\mathrm{D}t} = -\frac{1}{Ma}\nabla p + \frac{1}{Re}[\nabla^2\mathbf{v} + \tfrac{1}{3}\nabla(\nabla\cdot\mathbf{v})]. \tag{6}$$

We have $\Gamma = \Gamma_\mathrm{N} \cup \Gamma_\mathrm{S}$, where Γ_S denotes the wall boundaries and Γ_N denotes the moving boundary at the top of the cavity. No-slip conditions are imposed on all wall boundaries. On the top the boundary conditions are

$$u_i = 1 \quad \text{on } \Gamma_\mathrm{N}, \tag{7}$$

$$\tau_{ij}\cdot\mathbf{n} = 0 \quad \text{on } \Gamma_\mathrm{N}. \tag{8}$$

© 1998 John Wiley & Sons, Ltd.

2.2. Base flow

As the cavity is assumed to be infinitely long in the spanwise direction, the base flow whose stability is being examined is two-dimensional and steady, with the result that the equations for this flow simplify to

$$\nabla \cdot \mathbf{V} = 0 \quad \text{in } \Omega, \tag{9}$$

$$\mathbf{V} \cdot \nabla_* \mathbf{V} = -\nabla_* P + \frac{1}{Re} \nabla_*^2 \mathbf{V} \quad \text{in } \Omega, \tag{10}$$

where $\mathbf{V}$ and P are the velocity and kinematic pressure in the base flow respectively and ∇_* represents the two-dimensional gradient operator.

2.3. Perturbation equations

To investigate the stability of the base flow to disturbances, we need the equations that govern the evolution of these perturbations. To this end we perturb the base flow by a disturbance velocity $\mathbf{v}'$ and the pressure by p'. The total velocity and pressure are then written as

$$\mathbf{v} = \mathbf{V} + \mathbf{v}', \qquad p = P + p'. \tag{11}$$

Substituting (11) into the continuity equation (1) and the equation of motion (6), subtracting the base flow equations (9) and (10) and linearizing, we obtain the following equations for the perturbation velocity subject to no-slip conditions on all boundaries:

p'-equation

$$\frac{\mathrm{D}p'}{\mathrm{D}t} + (\mathbf{v}' \cdot \nabla) P + \frac{1}{Ma} \nabla \cdot \mathbf{v}' = 0 \quad \text{in } \Omega, \tag{12}$$

$\mathbf{v}'$-equations

$$\frac{\mathrm{D}\mathbf{v}'}{\mathrm{D}t} + (\mathbf{v}' \cdot \nabla)\mathbf{V} = -\frac{1}{Ma} \nabla p' + \frac{1}{Re} [\nabla^2 \mathbf{v}' + \tfrac{1}{3} \nabla (\nabla \cdot \mathbf{v}')] \quad \text{in } \Omega, \tag{13}$$

where the two-dimensional operator $\mathrm{D}/\mathrm{D}t = \partial/\partial t + \mathbf{V} \cdot \nabla_*$. The boundary conditions of the perturbances are

$$\mathbf{v}' = 0 \quad \text{on } \Gamma, \tag{14}$$

$$\left(-\frac{1}{Ma} p' \delta_{ij} + \frac{1}{Re} \left(\frac{\partial u_i'}{\partial x_j} + \frac{1}{3} \frac{\partial u_j'}{\partial x_j} \delta_{ij} \right) \right) \cdot n_j = 0 \quad \text{on } \Gamma_{\mathrm{N}}. \tag{15}$$

In terms of the normal mode we represent the disturbances of pressure and velocities in the symmetry plane and spanwise direction of the cavity as

$$p' = \mathrm{i}\hat{p}(x, y) \mathrm{e}^{\mathrm{i}\kappa z + \omega t}, \tag{16}$$

$$u' = \mathrm{i}\hat{u}(x, y) \mathrm{e}^{\mathrm{i}\kappa z + \omega t}, \tag{17}$$

$$v' = \mathrm{i}\hat{v}(x, y) \mathrm{e}^{\mathrm{i}\kappa z + \omega t}, \tag{18}$$

$$w' = \hat{w}(x, y) \mathrm{e}^{\mathrm{i}\kappa z + \omega t}, \tag{19}$$

where κ is the spanwise wave number and ω is the complex growth rate. The reason for the choice of the imaginary amplitude in normal modes is to avoid complex arithmetic in the subsequent

 © 1998 John Wiley & Sons, Ltd.

calculation of the eigenproblem. The assumed form of the eigenvector is completely general and allows for both steady and oscillatory modes, depending on whether the eigenvalue ω is real or complex respectively. According to linear stability theory, if ω is real, the disturbances either grow or decay monotonically; the critical Reynolds number is that for which $\omega = 0$. If ω is complex, the neutral condition is $\omega_r = 0$ and the onset of instability is oscillatory with dimensional wave speed ω_i. This normal mode form also includes the time-dependent two-dimensional instability of the steady flow for which $\kappa = 0$. Substituting these normal modes into (12) and (13) yields an eigenproblem with the growth rate being the eigenvalue:

$$\omega\hat{p} + (\mathbf{V}\cdot\nabla_*)\hat{p} + (\hat{\mathbf{v}}\cdot\nabla_*)P + M_a^{-1}(\nabla_*\cdot\hat{\mathbf{v}} + \kappa\hat{w}) = 0, \tag{20}$$

$$\omega\hat{u} + (\mathbf{V}\cdot\nabla_*)\hat{u} + (\hat{\mathbf{v}}\cdot\nabla_*)U + M_a^{-1}\frac{\partial\hat{p}}{\partial x} = Re^{-1}\left(\nabla_*^2\hat{u} - \kappa^2\hat{u} + \frac{1}{3}\frac{\partial}{\partial x}(\nabla_*\cdot\hat{\mathbf{v}} + \kappa\hat{w})\right), \tag{21}$$

$$\omega\hat{v} + (\mathbf{V}\cdot\nabla_*)\hat{v} + (\hat{\mathbf{v}}\cdot\nabla_*)V + M_a^{-1}\frac{\partial\hat{p}}{\partial y} = Re^{-1}\left(\nabla_*^2\hat{v} - \kappa^2\hat{v} + \frac{1}{3}\frac{\partial}{\partial y}(\nabla_*\cdot\hat{\mathbf{v}} + \kappa\hat{w})\right), \tag{22}$$

$$\omega\hat{w} + (\mathbf{V}\cdot\nabla_*)\hat{w} - M_a^{-1}\kappa\hat{p} = Re^{-1}[\nabla_*^2\hat{w} - \kappa^2\hat{w} - \tfrac{1}{3}\kappa(\nabla_*\cdot\hat{\mathbf{v}} + \kappa\hat{w})], \tag{23}$$

subject to no-slip conditions on all boundaries, i.e.

$$\hat{u} = \hat{v} = \hat{w} = 0 \quad \text{on } \Gamma, \tag{24}$$

and the stress condition

$$\left(-\frac{1}{Ma}\hat{p}\delta_{ij} + \frac{1}{Re}\left(\frac{\partial\hat{u}_i}{\partial x_j} + \frac{1}{3}\frac{\partial\hat{u}_j}{\partial x_j}\delta_{ij}\right)\right)\cdot n_j = 0 \quad \text{on } \Gamma_N. \tag{25}$$

2.4. Finite element formulations

For the discretization of (20)–(23) by means of the finite element method the interpolations for velocity and pressure eigenfunctions can be expressed as

$$\hat{\mathbf{v}} = \Phi_\alpha\hat{\mathbf{v}}_\alpha, \tag{26}$$

$$\hat{p} = \Phi_\alpha\hat{p}_\alpha, \tag{27}$$

where Φ_α is the interpolation function and $\hat{\mathbf{v}}_\alpha$ and $\hat{p}_\alpha$ represent the nodal values at the αth node of finite elements. The corresponding weighting functions are similar to (26) and (27). In our cases the linear interpolation function based on the linear triangular element for eigenfunctions is employed. After the superposition of element matrices the temporal mode of stability is expressed as the generalized eigenproblem

$$\mathbf{A}\Phi = \omega\mathbf{B}\Phi, \tag{28}$$

where $\mathbf{B}$ is the assembling consistent mass matrix and $\Phi = \{\hat{u}, \hat{v}, \hat{w}, \hat{p}\}^T$ is the assembling vector of eigenfunctions. If N is the total number of nodal points and N_b is the number of nodal points on all no-slip boundaries, the dimensions of the square matrices $\mathbf{A}$ and $\mathbf{B}$ can be reduced to $4(N - N_b)$ through column operations. This indicates that the ranks of $\mathbf{A}$ and $\mathbf{B}$ are $4(N - N_b)$.

3. NUMERICAL METHODS

In this section the numerical methods used to compute the base flow and solve the eigenproblem for the identification of the critical state are described.

© 1998 John Wiley & Sons, Ltd.

3.1. Base flow computations

The evaluation of two-dimensional base flows is performed using the improved velocity correction method with the continuity constraint by means of the finite element method.[14] Such methods based on the fractional step scheme have been investigated widely; see Reference 16 for the finite difference method and References 17 and 18 for the finite element method. The results from various numerical methods for two-dimensional cavity flow show good accuracy in comparison with the experimental data. After numerical experiments to determine the appropriate grid size, we found that at the lower Reynolds numbers (i.e. below $Re = 300$) a 33×33 grid was adequate for obtaining grid-invariant results and for the higher Reynolds numbers a finer 81×81 grid was necessary. For the sake of computational simplicity an 81×81 non-uniform grid is used for the simulation of steady flows in all cases. Details of the solution methodology for a related problem have been reported elsewhere.[14] Figure 1(a) shows the flow structure at $Re = 1000$, which consists of a primary vortex, secondary vortices at the bottom corners and an incipient vortex at the upper left-hand corner. Figure 1(b) presents the steady distribution of pressure at this Reynolds number.

The fluid is considered as water in this case. The base flows were computed by double-precision arithmetic at discrete values of Re of 50, 100, 200, 300, 400, 500, 600, 700, 800, 900, 1000, 1020, 1030, 1050, 1100, 1200 and 1500 on grids as fine as 81×81.

3.2. Solution of eigenproblem

In the generalized eigenproblem (28) the eigenvalue pencil of the real unsymmetric matrix contains real values and complex conjugate pairs. To detect the onset of instability, we need to identify the eigenvalues closest to the imaginary axis. The leading or dominant eigenvalues that we seek are those with maximum real part. In this subsection we will discuss briefly the traditional QR method and Arnoldi's method with the 'shift and invert' strategy.

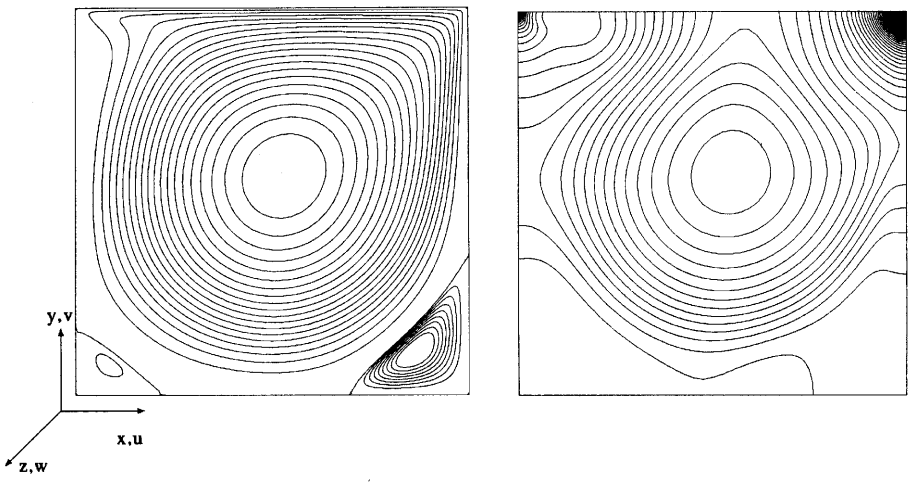

(a) Streamlines (Ψ_{max}=1.716E-3, Ψ_{min}=-0.119) (b) Isobars (P_{max}=0.708, P_{min}=-0.122)

Figure 1. 2D steady flow at $Re = 1000$

 © 1998 John Wiley & Sons, Ltd.

3.2.1. QR method. Although the QR method is very expensive for the computation of all eigenvalues, it is effective and accurate for the detection of eigenvalues in an unsymmetric eigenproblem. In particular, for (28) in our case the matrix **A** has a large condition number and is a ill-conditioned matrix. Thus it is reasonable to use the QR method to detect an eigenspectrum in advance so as to recognize the basic characteristics of eigenproblem (28) subject to the slight compressibility assumption.

As the matrix **B** in (28) is symmetric and positive definite, before calculating the spectrum in (28), this problem is most efficiently solved by reduction to a standard eigenproblem by Cholesky factorization of $\mathbf{B} = L^{\mathrm{T}}L$. Thus one can obtain the standard eigenproblem

$$\mathbf{H}z = \omega z, \quad \text{with } z = L\Phi, \tag{29}$$

where $\mathbf{H} = L^{-\mathrm{T}}\mathbf{A}L^{-1}$ is a transformed matrix of **A**; see Reference 19 for a detailed description of this transformation.

3.2.2. Arnoldi's method with 'shift and invert' strategy. For the standard eigenvalue problem $\mathbf{C}\Phi = \omega\Phi$, in order to compute the *dominant* eigenvalue ω_1 of **C** ($|\omega_1| > |\omega_j|$ for $j = 2, \ldots, N$), a brief description of Arnoldi's method is as follows.[20,21]

Arnoldi's algorithm as a purification process

1. *Start*. Choose an initial vector v_1 of unity norm and a number of steps m.
2. *Iterate*. For $j = 1, 2, \ldots, m$ do

$$\hat{v}_{j+1} = \mathbf{C}v_j - \sum_{i=1}^{j} h_{ij}v_i, \tag{30}$$

with

$$h_{ij} = (\mathbf{C}v_j, v_i), \quad i = 1, \ldots, j, \tag{31}$$

$$h_{j+1,j} = \|\hat{v}_{j+1}\|, \tag{32}$$

$$v_{j+1} = \hat{v}_{j+1}/h_{j+1,j}. \tag{33}$$

This algorithm produces an orthonormal basis $\mathbf{V}_m = [v_1, v_2, \ldots, v_m]$ of the Krylov subspace $\mathbf{K}_m = \mathrm{span}\{v_1, \mathbf{C}v_1, \ldots, \mathbf{C}^{m-1}v_1\}$. In this basis the restriction of **C** to $\mathbf{K}_m$ is represented by the upper Hessenberg matrix $\mathbf{H}_m$ whose entries are the h_{ij} produced by the algorithm, i.e.

$$\mathbf{H}_m = \{h_{ij}\}. \tag{34}$$

The eigenvalues of **C** are approximated by those of $\mathbf{H}_m$, which is such that

$$\mathbf{H}_m = \mathbf{V}_m^{\mathrm{T}}\mathbf{C}\mathbf{V}_m. \tag{35}$$

The associated approximate eigenvectors are given by

$$\tilde{\Phi}_i = \mathbf{V}_m\tilde{y}_i, \tag{36}$$

where $\tilde{y}_i$ is an eigenvector of $\mathbf{H}_m$ associated with the eigenvalue $\tilde{\omega}_i$. Note that $\tilde{\Phi}_i$ has the same Euclidean norm as $\tilde{y}_i$. The following relation is extremely useful for obtaining the residual norm of $\tilde{\Phi}_i$ without computing it explicitly:

$$\|(\mathbf{C} - \tilde{\omega}_i I)\tilde{\Phi}_i\|_2 = h_{m+1,m}|e_m^{\mathrm{T}}\tilde{y}_i|, \tag{37}$$

in which $e_m = (0, 0, \ldots, 0, 1)^{\mathrm{T}}$.

© 1998 John Wiley & Sons, Ltd.

Shift and invert for (28)

In order to find the leading eigenvalue with maximum real part, one can use the 'shift and invert' strategy.[22] If ω_0 is an approximation to an eigenvalue of interest, the shifted and inverted eigenproblem is

$$(\mathbf{C} - \omega_0 I)^{-1}\Phi = \lambda\Phi, \tag{38}$$

where $\lambda = 1/(\omega - \omega_0)$. In order to apply Arnoldi's method to (38) for the generalized eigenproblem (28), we do not wish to form $\mathbf{C} = \mathbf{B}^{-1}\mathbf{A}$. Rather, (38) may be written as

$$(\mathbf{A} - \omega_0\mathbf{B})^{-1}\mathbf{B}\Phi = \lambda\Phi. \tag{39}$$

Thus we need to solve a linear algebraic equation at each Arnoldi step as

$$(\mathbf{A} - \omega_0\mathbf{B})w_j = \mathbf{B}v_j \quad (j = 2, 3, \ldots, m). \tag{40}$$

Because of the ill-conditioned matrix $\mathbf{A}$, we choose two strategies to solve the above equation. One approach is to form the inverse matrix $(\mathbf{A} - \omega_0\mathbf{B})^{-1}$ only once in Arnoldi's iteration. Another is to solve it by a direct solver such as LU decomposition with partial pivoting. However, the eigenvalues obtained by the latter method show that the condition number of $\mathbf{A}$ is so large that the eigenspectrum is seriously distorted; in addition, the shifted value ω_0 should be chosen very small so as to avoid the distortion of eigenvalues. Therefore it follows that only the direct inverse matrix solver and purified inverse process are effective for our eigenproblem (28).

4. NUMERICAL RESULTS FOR CAVITY FLOW

In this section we present our results for driven cavity flow. As mentioned above, the base flows were computed as a discrete series and used for stability computation. Since the computed fluid is water as stated above, in the computation of the eigenproblem we considered this fluid with a physical compressibility where the acoustic speed was chosen as 1449·36 m s^{-1} in correspondence with the general situation of a fluid at a temperature of 10·0 °C. Therefore the range of Mach numbers is from $4{\cdot}5 \times 10^{-7}$ to $1{\cdot}4 \times 10^{-5}$. This means that the slight compressibility assumption possesses a physical character in our cases, in contrast with the choice of an artificial compressibility parameter by Malik and Poll[5] and Khorrami *et al.*[6] For the calculation of eigenvalues, owing to the memory limitation of our computer, we performed grid convergence tests on grids from 11×11 to 21×21. We found that for the lower Reynolds numbers a 21×21 non-uniform grid was adequate for obtaining grid-invariant results.

4.1. Comparison of results from QR and Arnoldi methods

We first computed a spectrum of cavity flow at $Re = 50$ by means of the QR method and found an approximated one at the same Reynolds number by the inverted Arnoldi method with step $m = 60$. The CPU time on an IBM RS/6000 is 235 min for computation by the QR method but only 200 s for that by Arnoldi's method with $m = 60$. Thus we can say that Arnoldi's method is much more effective than the QR method despite the adoption of a direct inverse matrix solver in Arnoldi's method.

Figure 2 shows the distribution of spectra from the two methods. The leading part of the approximated spectrum is in good agreement with that part by the QR method. In order to obtain an adequate number of Arnoldi steps, we compare the residual norm of spectra in Figure 3 for $Re = 400$ with $\kappa = 2$ from $m = 20$ to 60. It follows that the residual norm of leading eigenvalues can be kept in the range from 10^{-16} to 10^{-18}. If one specifies the criteria that the norm is less than 10^{-10} and only three leading eigenvalues are necessary, an adequate number of Arnoldi steps will be no more than

 © 1998 John Wiley & Sons, Ltd.

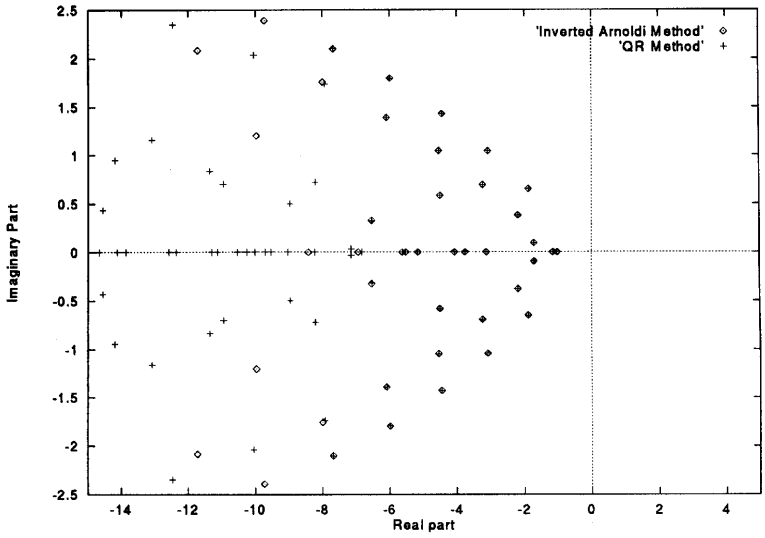

Figure 2. Comparison of eigenvalue distribution at $Re = 50$ and $\kappa = 2$

30. This means that only 150 s of CPU time is needed to obtain the eigenvalues and corresponding eigenfunctions of interest.

4.2. *Validation of stability results*

In order to validate the stability result with three-dimensional perturbation by means of the inverted Arnoldi method, we compared it with that of Ramanan and Homsy[2] in which the

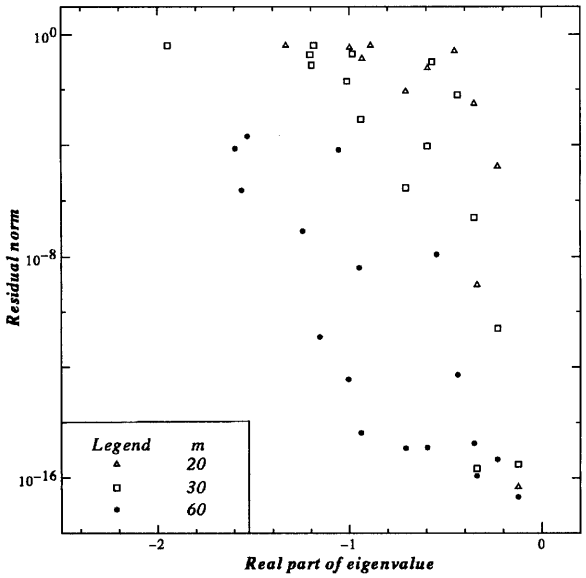

Figure 3. Convergence of Arnoldi's method at various steps

© 1998 John Wiley & Sons, Ltd.

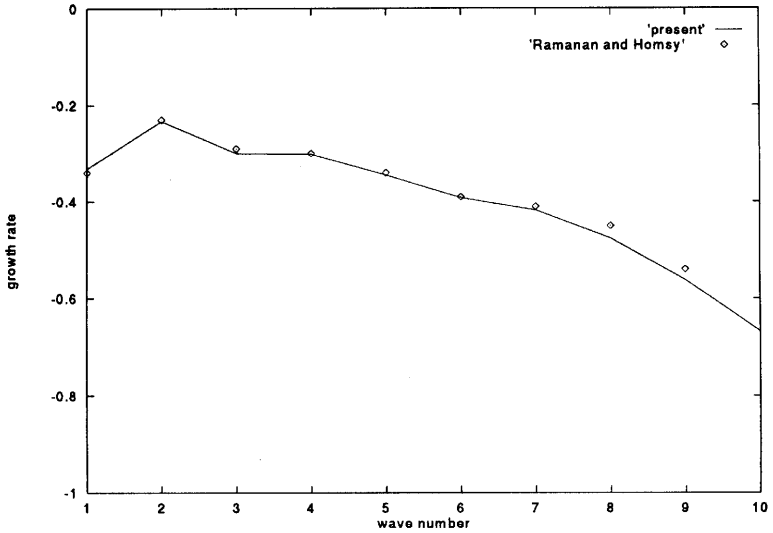

Figure 4. Comparison of real part versus wave number at $Re = 200$

perturbation equations are a type of potential functions in three-dimensional disturbances, the discrete method is finite difference and the spectra of cavity flows were determined by means of the simultaneous iteration method.[23] We show the comparison of maximum real and corresponding imaginary parts at $Re = 200$ with those of Ramanan and Homsy[2] in Figures 4 and 5 respectively. We see that the present results from the finite element method are very close to those from the finite difference method at the lower Reynolds numbers (i.e. below $Re = 400$). It can be seen that the stability results incorporating slight compressibility have good accuracy despite the coarse 21×21 grid (in this work a 31×31 grid was employed to determine the stability curve).

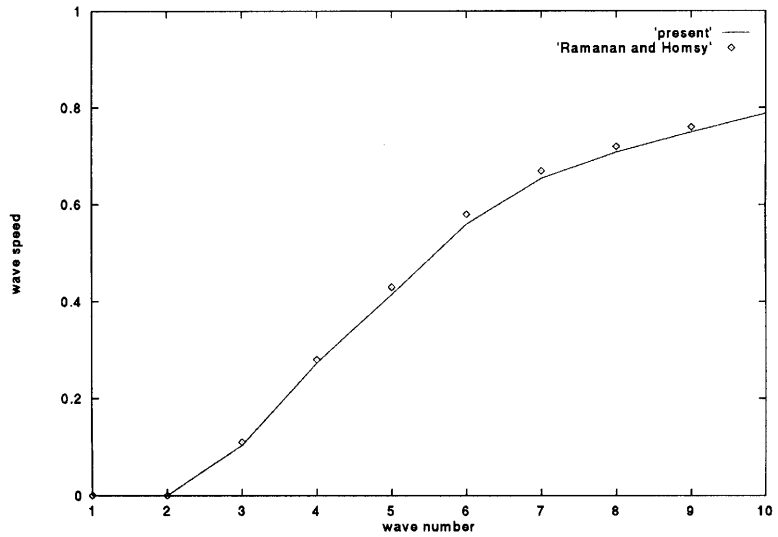

Figure 5. Comparison of imaginary part versus wave number at $Re = 200$

 © 1998 John Wiley & Sons, Ltd.

Table I. Leading eigenvalue (ω) versus wave number (κ) for various Reynolds numbers

κ	$Re = 100$	$Re = 400$	$Re = 700$	$Re = 1030$
1	$-0{\cdot}52678$	$-0{\cdot}22312 \pm 0{\cdot}25754i$	$-0{\cdot}12364 \pm 0{\cdot}26650i$	$-0{\cdot}08452 \pm 0{\cdot}26675i$
2	$-0{\cdot}47243$	$-0{\cdot}12232$	$-0{\cdot}09801$	$-0{\cdot}08594 \pm 0{\cdot}51788i$
3	$-0{\cdot}52733$	$-0{\cdot}14580 \pm 0{\cdot}15299i$	$-0{\cdot}08344 \pm 0{\cdot}17770i$	$-0{\cdot}05827 \pm 0{\cdot}18274i$
4	$-0{\cdot}60984 \pm 0{\cdot}17367i$	$-0{\cdot}13392 \pm 0{\cdot}30691i$	$-0{\cdot}07771 \pm 0{\cdot}31785i$	$-0{\cdot}07290 \pm 0{\cdot}31379i$
5	$-0{\cdot}70117 \pm 0{\cdot}29734i$	$-0{\cdot}17752 \pm 0{\cdot}44775i$	$-0{\cdot}10313 \pm 0{\cdot}58930i$	$-0{\cdot}03714 \pm 0{\cdot}56215i$
6	$-0{\cdot}81605 \pm 0{\cdot}40938i$	$-0{\cdot}14934 \pm 0{\cdot}61269i$	$-0{\cdot}04978 \pm 0{\cdot}59220i$	$-0{\cdot}02144 \pm 0{\cdot}53865i$
7	$-0{\cdot}94911 \pm 0{\cdot}50357i$	$-0{\cdot}15101 \pm 0{\cdot}64775i$	$-0{\cdot}07185 \pm 0{\cdot}55929i$	$-0{\cdot}00030 \pm 0{\cdot}49996i$
8	$-1{\cdot}10263 \pm 0{\cdot}58012i$	$-0{\cdot}22922 \pm 0{\cdot}67453i$	$-0{\cdot}07235 \pm 0{\cdot}51982i$	$-0{\cdot}00130 \pm 0{\cdot}47186i$
9	$-1{\cdot}27645 \pm 0{\cdot}64284i$	$-0{\cdot}25985 \pm 0{\cdot}56246i$	$-0{\cdot}08678 \pm 0{\cdot}49409i$	$-0{\cdot}01155 \pm 0{\cdot}45308i$
10	$-1{\cdot}46985 \pm 0{\cdot}06940i$	$-0{\cdot}28927 \pm 0{\cdot}53142i$	$-0{\cdot}11243 \pm 0{\cdot}48171i$	$-0{\cdot}03889 \pm 0{\cdot}45148i$

Other similar results at selected Reynolds numbers from $Re = 100$ to 1030 are listed in Table I. Apart from some of the leading eigenvalues at the smaller Reynolds numbers and lower wave numbers κ, most of these dominant eigenvalues are Hopf modes followed by some real eigenvalues and complex conjugate pairs and all modes are damped.

4.3. Dispersion relation

Figure 6 shows our principal results $\omega_r(\kappa, Re)$ for the maximum real part (growth rate) of eigenvalues. Over the range of Reynolds numbers the growth rate in Figure 6 shows a critical situation at $Re = 1030$ with $\kappa = 8$. In Figure 7 it is found that the $\kappa = 8$ mode crosses the imaginary axis first and is immediately followed by the $\kappa = 7$ mode at a slightly higher Reynolds number. We do not find that the $\kappa = 5$ mode crosses the imaginary axis in the discrete sequence of these cavity flows as was reported by Ramanan and Homsy.[2] To obtain the critical Reynolds number for any given wave number, we performed an interpolation for various wave numbers. We estimated the critical Reynolds number as 1025 at a critical wave number of 7·6. In Table I it is also noted that the critical mode is a Hopf mode. From Figure 8 the corresponding wave speed ω_i was estimated as 0·5, which means that this mode has a non-dimensional wavelength of 0·84, close to unity (i.e. the width or height of the cavity), and a dimensionless frequency ($= \omega_i/2\pi$) of 0·08. This result is very close to the observation of Aidun *et al.*,[13] whose estimate of the critical Reynolds number is between 825 and 925. The critical Reynolds numbers in our cases are $O(1000)$ for three-dimensional perturbation, while they are $O(7000)$ for two-dimensional modes computed by Poliashenko and Aidun, as reported by Ramanan and Homsy.[2] This implies that all the three-dimensional modes are significantly more unstable than the two-dimensional modes ($\kappa = 0$).

In addition, Figure 9 presents the (a) real and (b) imaginary parts of the velocity disturbance in the symmetry plane at $Re = 1030$ with $\kappa = 8$ for the leading eigenvalue with the smallest growth rate.

4.4. Reconstruction of 3D flow

In order to reproduce the three-dimensional flow field that corresponds to the critical mode, we reconstructed the total three-dimensional flow field by combining the two-dimensional base flow with

© 1998 John Wiley & Sons, Ltd.

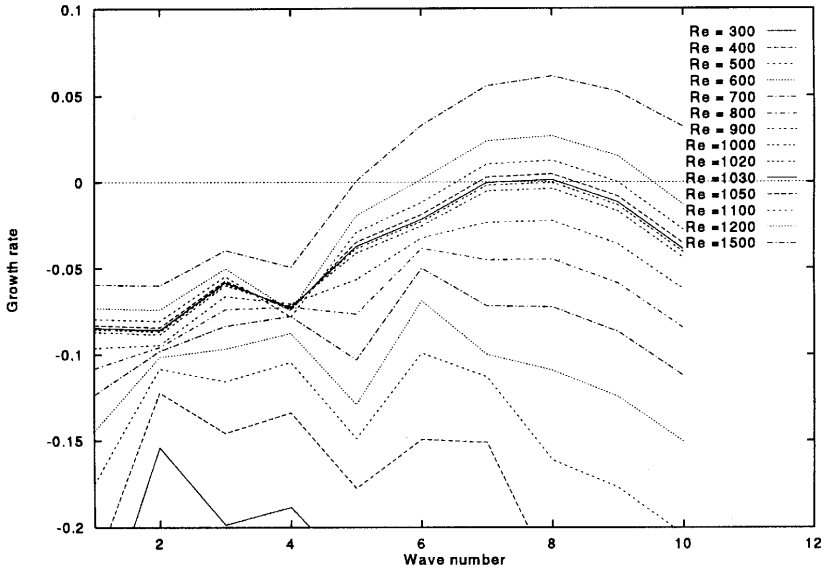

Figure 6. Growth rate versus wave number at various *Re*

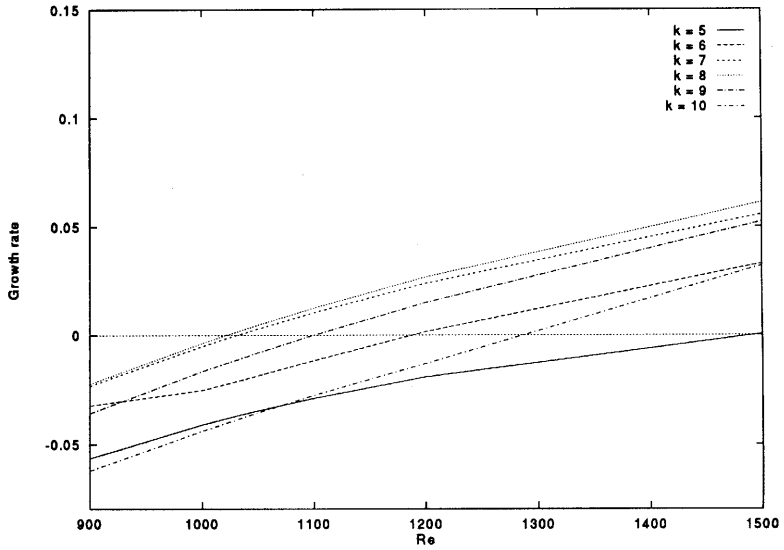

Figure 7. Growth rate versus *Re*

 © 1998 John Wiley & Sons, Ltd.

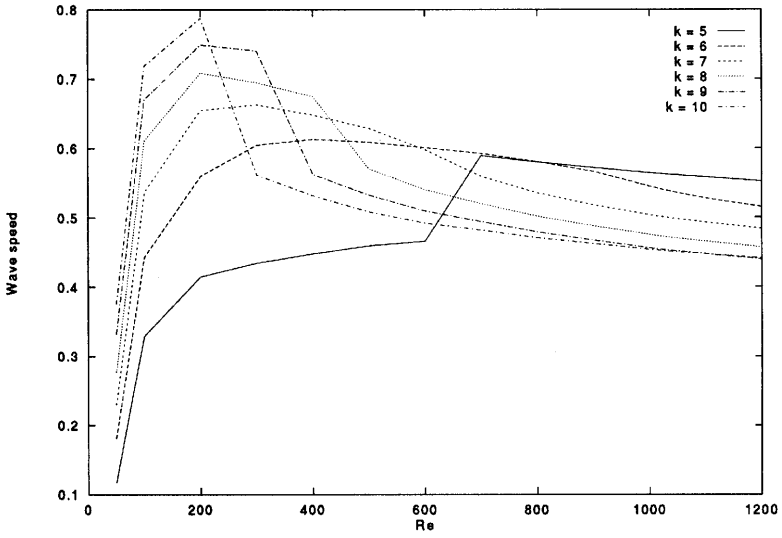

Figure 8. Wave speed versus *Re*

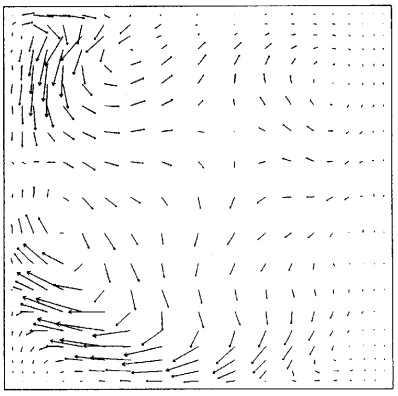

(a) Real Part

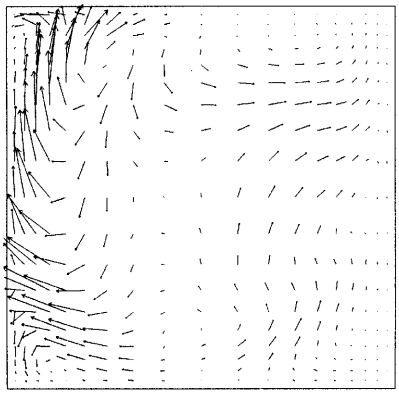

(b) Imaginary part

Figure 9. Velocity disturbance in symmetry plane at $Re = 1030$ with $\kappa = 8$

© 1998 John Wiley & Sons, Ltd.

an arbitrary amount of the disturbance eigenvector. Considering the conjugate pairs of the eigenspectrum, the reconstructed flow is the following superposition of eigenvectors:

$$u = U - 2\sum_{n=1}^{N_t} e^{\omega_r^n t}\{\cos(\kappa z)[\hat{u}_i^n \cos(\omega_i^n t) + \hat{u}_r^n \sin(\omega_i^n t)] + i\sin(\kappa z)[\hat{u}_i^n \cos(\omega_i^n t) + \hat{u}_r^n \sin(\omega_i^n t)]\}, \tag{41}$$

$$v = V - 2\sum_{n=1}^{N_t} e^{\omega_r^n t}\{\cos(\kappa z)[\hat{v}_i^n \cos(\omega_i^n t) + \hat{v}_r^n \sin(\omega_i^n t)] + i\sin(\kappa z)[\hat{v}_i^n \cos(\omega_i^n t) + \hat{v}_r^n \sin(\omega_i^n t)]\}, \tag{42}$$

$$w = 2\sum_{n=1}^{N_t} e^{\omega_r^n t}\{\cos(\kappa z)[\hat{w}_i^n \cos(\omega_i^n t) - \hat{w}_r^n \sin(\omega_i^n t)] + i\sin(\kappa z)[\hat{w}_r^n \cos(\omega_i^n t) - \hat{w}_i^n \sin(\omega_i^n t)]\}, \tag{43}$$

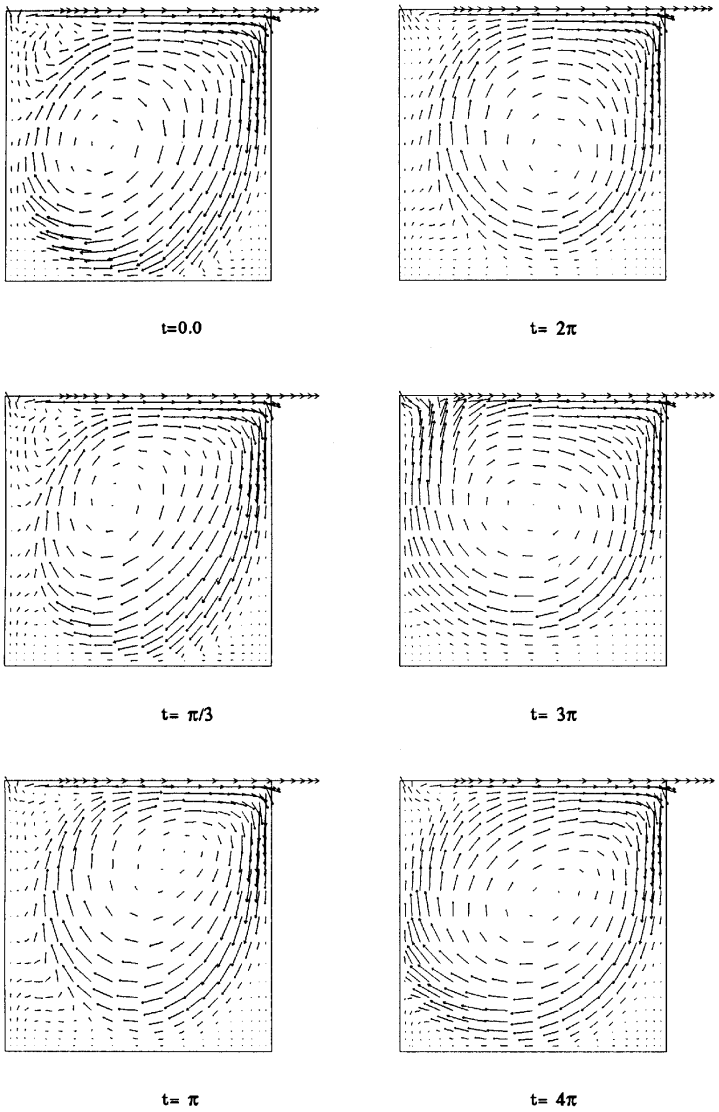

Figure 10. Evolution of reconstructed flow planes at $z = 0$ and $Re = 1030$ with $\kappa = 8$

 © 1998 John Wiley & Sons, Ltd.

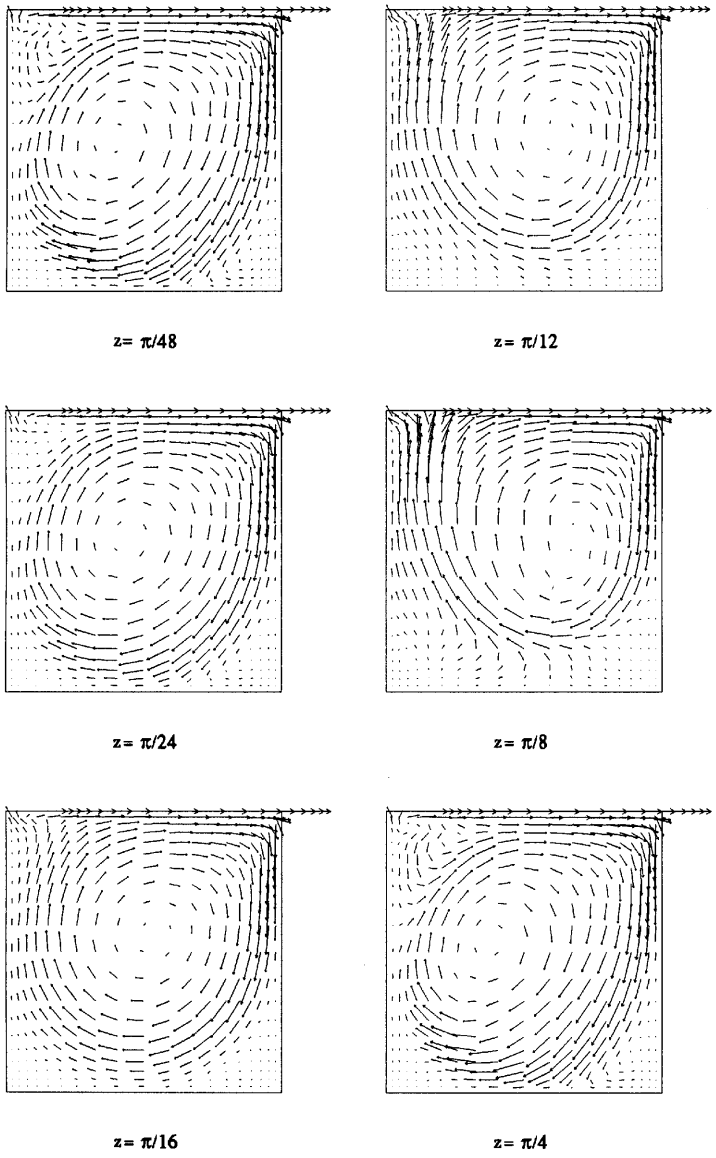

Figure 11. Views of reconstructed flows in spanwise planes at $t=\pi/24$ and $Re=1030$ with $\kappa=8$

where the subscript 'r' denotes the real part of an eigenvalue or eigenvector and the subscript 'i' denotes the imaginary part. In terms of the superposition using four pairs of eigenvectors, in the critical mode (i.e. $Re=1030$ with $\kappa=8$) including the leading pair (i.e. $N_t=4$ in (41) and (42)), we illustrate the temporal flow patterns (real part) in the symmetry plane $z=0$ for the critical mode in Figure 10 (temporal mode). The three-dimensional effect for the spanwise midplane $z=0$ is seen very vividly. Among the temporal flow fields from dimensionless time $t=0{\cdot}0$ to 4π it can be clearly observed that oscillation of the primary vortex occurs in which the average dimensionless frequency is close to 0·10. Similar three-dimensional flow patterns can be found in Reference 24 based on numerical simulation by a finite difference method and in Reference 25 by a finite element code (N3S

© 1998 John Wiley & Sons, Ltd.

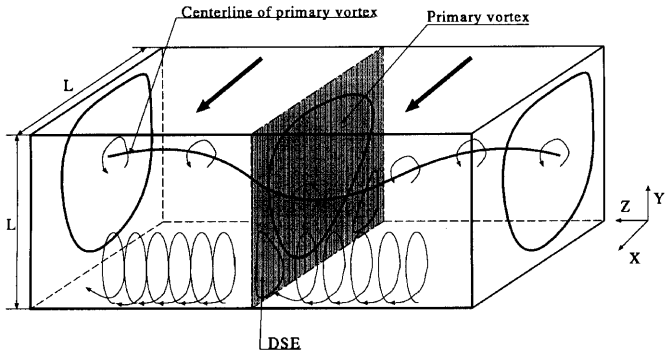

Figure 12. Schematic illustration of time-periodic vortex for three-dimensional cavity flow

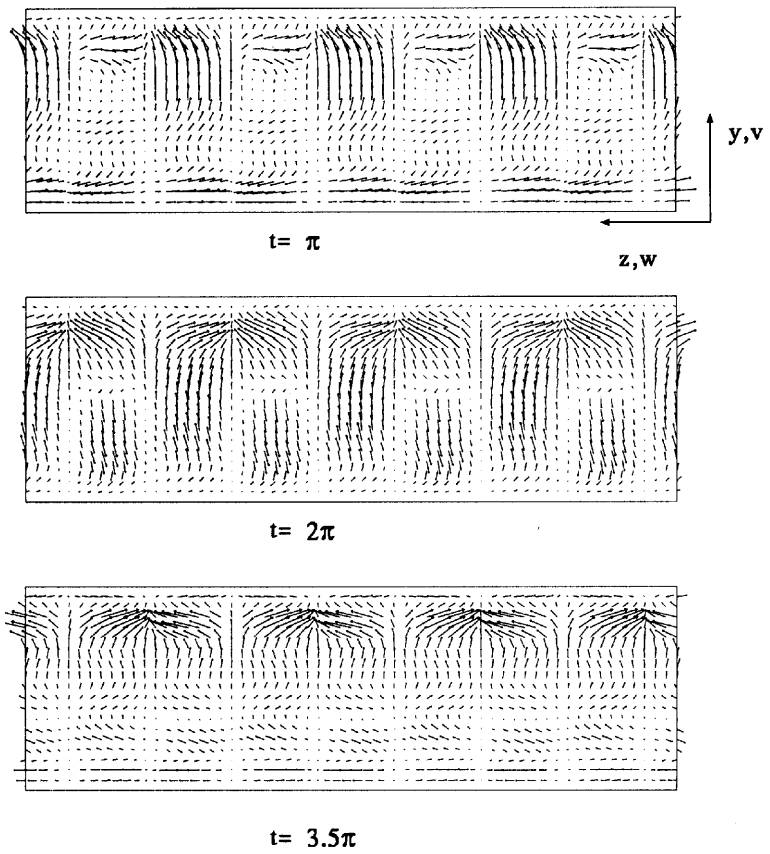

Figure 13. Evolution of velocity fields in y–z plane at $x = L/2$ and $Re = 1030$ with $\kappa = 2$

 © 1998 John Wiley & Sons, Ltd.

code). We plot further the reconstructed flows in various spanwise planes at dimensionless time $t=\pi/24$ for the critical mode in Figure 11 (spatial mode). It is found that the centreline of the primary vortex oscillates spatially in a sinuous way in the spanwise direction. To sum up the above description of the reconstructed flow pattern, a schematic diagram of this three-dimensional structure is depicted in Figure 12. It reappears that in the temporal mode, spiral-shaped vortices are superimposed on the primary vortex and downstream secondary eddy (DSE) travelling from the symmetry plane outward in the spanwise direction. The disturbance structure near the critical mode is more visible in the DSE than in the primary vortex. The motion of these vortices is similar to the rotation of a spring around its axis. These results have been proven in the experiments of Aidun *et al.*[13]

To verify the existence of Taylor–Göertler-like (TGL) vortices in the spanwise plane, which are frequently described in numerical simulations[16,24,25] and experiments,[13] we present the development of the spanwise velocity fields in the symmetry plane for the critical mode in Figure 13. The spanwise fields consist of a mushroom-like structure travelling from the symmetry plane outward in the spanwise direction. Similar structures were observed in flow visualizations by Aidun *et al.*[13] The contours of the normal velocity (ω_x) are presented temporally in Figure 14. They show a cellular structure which has a dimensionless wavelength of $\pi/4$ (Aidun *et al.*[13] reported an average wavelength of half the cavity width, while Kim and Moin[16] showed numerically two pairs of TGL

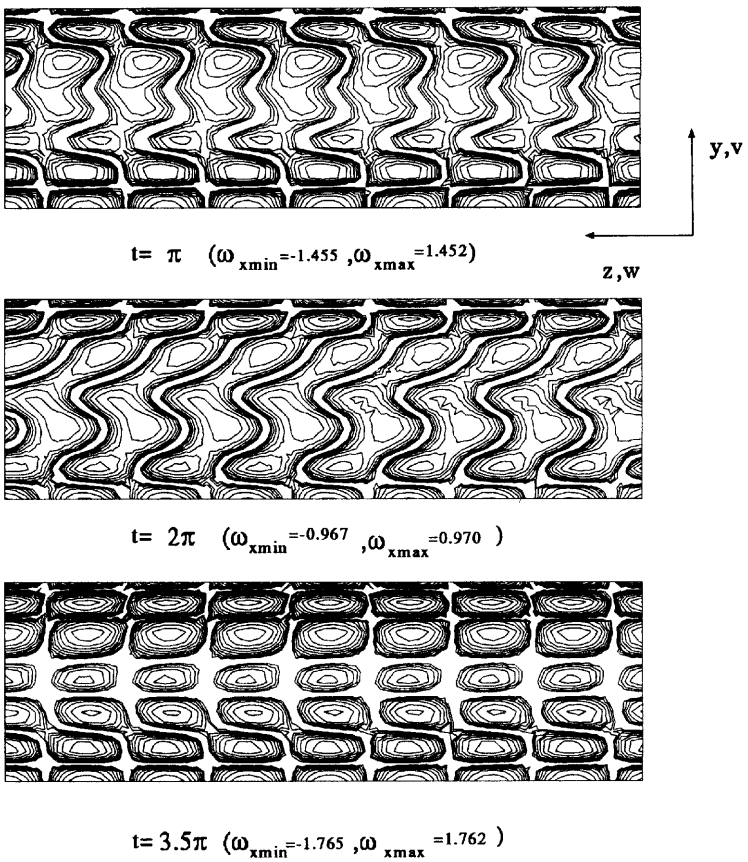

Figure 14. Evolution of normal vorticity fields in y–z plane at $x=L/2$ and $Re=1030$ with $\kappa=2$

© 1998 John Wiley & Sons, Ltd.

vortices per cavity width at $Re = 1000$). As the ordered cellular structure breaks down, a transition to turbulence in the cavity flow will occur.

5. CONCLUSIONS

In this paper we have investigated the linear stability of incompressible fluid flow in a lid-driven cavity by means of the assumption of a slight compressibility forced in the Navier–Stokes equations. From the obtained results our conclusions are as follows.

1. It is reasonable to use a compressibility with physical meaning to reduce the singularity in the generalized eigenproblem which occurs in the linear stability of incompressible fluid flow.
2. The inverted Arnoldi method is very effective to detect the dominant parts of eigenvalues. In addition, the ill-conditioning difficulty in the eigenproblem can be effectively overcome by use of a direct inverse solver with partial pivoting; a higher accuracy of eigenvectors can thus be maintained.
3. The estimated critical results in this case are 1025 for the Reynolds number and 7·6 for the critical wave number, for which a non-dimensional frequency of 0·8 is found. These results are close to the observations of Aidun *et al.*[13]
4. By means of reconstruction of flows in the critical mode, the three-dimensionality in the cavity flow reappears. These results show that the TGL vortices play a key role in generating three-dimensional flow patterns in the cavity.
5. Because of the physical compressibility assumed in the perturbation equations in our cases, the present method can also be used for the stability analysis of real compressible fluid flows.

REFERENCES

1. P. Huerre and P. A. Monkewitz, 'Local and global instabilities in spatially developing flows', *Ann. Rev. Fluid Mech.*, **22**, 473–537 (1990).
2. N. Ramanan and G. M. Homsy, 'Linear stability of lid-driven cavity flow', *Phys. Fluids*, **6**, 2690–2701 (1994).
3. S. A. Orszag, 'Accurate solution of the Orr–Sommerfeld stability equation', *J. Fluid Mech.*, **50**, 689–703 (1971).
4. L. Kleiser and T. A. Zang, 'Numerical simulation of transition in well-bounded shear flows', *Ann. Rev. Fluid Mech.*, **23**, 495–537 (1991).
5. M. R. Malik and D. I. A. Poll, 'Effect of curvature on three-dimensional boundary-layer stability', *AIAA J.*, **23**, 1362–1369 (1985).
6. M. R. Khorrami, M. R. Malik and R. L. Ash, 'Application of spectral collocation techniques to the stability of swirling flows', *J. Comput. Phys.*, **81**, 206–229 (1989).
7. M. R. Malik, 'Numerical methods for hypersonic boundary layer stability', *J. Comput. Phys.*, **86**, 376–413 (1990).
8. M. Morzynski and F. Thiele, 'Numerical stability analysis of a flow about a cylinder', *Z. Angew. Math. Mech.*, **71**, T424–T428 (1991).
9. M. Morzynski and F. Thiele, 'Numerical investigation of wake instabilities', in H. Eckelman, J. M. R. Graham, P. Huerre and P.A. Monkewitz (eds), *Bluff-Body Wakes, Dynamics and Instabilities*, Spring, Berlin, 1992, pp. 135–142.
10. Y. S. Li and S. C. Kot, 'One-dimensional finite element method in hydrodynamic stability', *Int. j. numer. methods eng.*, **17**, 853–870 (1981).
11. C. P. Jackson, 'A finite-element study of the onset of vortex shedding in flow past variously shaped bodies', *J. Fluid Mech.*, **182**, 23–45 (1987).
12. D. S. Malkus, 'Eigenproblems associated with the discrete LBB condition for incompressible finite elements', *Int. J. Eng. Sci.*, **19**, 1299–1310 (1981).
13. C. K. Aidun, N. G. Triantafillopoulos and J. D. Benson, 'Global stability of lid-driven cavity with throughflow: flow visualization studies', *Phys. Fluids A*, **3**, 2081–2091 (1991).
14. Y. Ding and M. Kawahara, 'Improved velocity correction method with constraint of continuity using finite element method', *Proc. Conf. on Comput. Engineering and Science*, Vol. 1, pp. 373–376, JSCES, Tokyo, 1996.
15. R. Kessler, 'Non-linear transition in three dimensional convection', *J. Fluid Mech.*, **174**, 357–379 (1987).
16. J. Kim and P. Moin, 'Application of a fractional-step method to incompressible Navier–Stokes equations', *J. Comput. Phys.*, **59**, 308–323 (1985).

 © 1998 John Wiley & Sons, Ltd.

17. C. B. Jiang and M. Kawahara, 'A three-step finite element method for unsteady incompressible flows', *Comput. Mech.*, **11**, 355–370 (1993).
18. D. M. Hawken, H. R. Tamaddon-Jahromi, P. Townsend and M. F. Webster, *Int. j. numer. methods fluids*, **10**, 327–351 (1990).
19. M. Kawahara and Y. Ding, 'Bifurcation analysis of brown tide by reaction–diffusion equation using finite element method', *J. Comput. Phys.*, **131**, 253–266 (1997).
20. W. E. Arnoldi, 'The principle of minimized iterations in the solution of the matrix eigenvalues problem', *Q. Appl. Math.*, **9**, 17–29 (1951).
21. Y. Saad, 'Variations on Arnoldi's method for computing eigenelements of large unsymmetric matrices', *Lin. Alg. Appl.*, **34**, 269–295 (1980).
22. N. Nayar and J. M. Ortega, 'Computation of selected eigenvalues of generalized eigenvalue problems', *J. Comput. Phys.*, **108**, 8–14 (1993).
23. W. J. Stewart and A. Jennings, 'A simultaneous iteration algorithm for real matrices', *ACM Trans. Math. Softw.*, **7**, 184–198 (1981).
24. Y. Huang, U. Ghia, G. A. Osswald and K. N. Ghia, 'Velocity–vorticity simulation of unsteady 3-D viscous flow within a driven cavity', in M. Deville, T.-H. Lê and Y. Morchoisne (eds), *Numerical Simulation of 3-D Incompressible Unsteady Viscous Laminar Flows*, NNFM Vol. 36, Vieweg, Braunschweig, 1992, pp. 54–66.
25. L. Janvier, B. Metivet, R. Mgouni, G. Pot and E. Razafindrakoto, 'A 3-D driven cavity flow simulation with N3S code', in M. Deville, T.-H. Lê and Y. Morchoisne (eds), *Numerical Simulation of 3-D Incompressible Unsteady Viscous Laminar Flows*, NNFM Vol. 36, Vieweg, Braunschweig, 1992, pp. 54–66.

© 1998 John Wiley & Sons, Ltd.